

---

# **An Experimental Investigation of the Flow Over the Rear End of a Notchback Automobile Configuration**

**Luther N. Jenkins**  
NASA Langley Research Center

Reprinted From: **Vehicle Aerodynamics**  
(SP-1524)

SAE routinely stocks printed papers for a period of three years following date of publication. Direct your orders to SAE Customer Sales and Satisfaction Department.

Quantity reprint rates can be obtained from the Customer Sales and Satisfaction Department.

To request permission to reprint a technical paper or permission to use copyrighted SAE publications in other works, contact the SAE Publications Group.



**GLOBAL MOBILITY** DATABASE

*All SAE papers, standards, and selected books are abstracted and indexed in the Global Mobility Database*

**ISSN 0148-7191**

Positions and opinions advanced in this paper are those of the author(s) and not necessarily those of SAE. The author is solely responsible for the content of the paper. A process is available by which discussions will be printed with the paper if it is published in SAE Transactions. For permission to publish this paper in full or in part, contact the SAE Publications Group.

Persons wishing to submit papers to be considered for presentation or publication through SAE should send the manuscript or a 300 word abstract of a proposed manuscript to: Secretary, Engineering Meetings Board, SAE.

**Printed in USA**

# An Experimental Investigation of the Flow Over the Rear End of a Notchback Automobile Configuration

Luther N. Jenkins

NASA Langley Research Center

## ABSTRACT

An experimental investigation of the flow over the rear end of a 0.16 scale notchback automobile configuration has been conducted in the NASA Langley Basic Aerodynamics Research Tunnel (BART). The objective of this work was to investigate the flow separation that occurs behind the backlight and obtain experimental data that can be used to understand the physics and time-averaged structure of the flow field. A three-component laser velocimeter was used to make non-intrusive, velocity measurements in the center plane and in a single cross-flow plane over the decklid. In addition to off-body measurements, flow conditions on the car surface were documented via surface flow visualization, boundary layer measurements, and surface pressures. The experimental data show several features previously identified by other researchers, but also reveal differences between the flow field associated with this particular configuration and the generally accepted models for the flow over a notchback rear end.

## INTRODUCTION

The aerodynamic performance of an automobile is largely determined by its drag coefficient and overall stability when subjected to cross winds and gusts. Because drag also influences engine requirements and fuel consumption, designers and engineers work to develop automotive shapes that are both aesthetically appealing and functional yet produce minimal drag. This task becomes somewhat paradoxical in that many designs that are aesthetically appealing and functional promote flow separation, which increases drag. Despite this constraint, designers and engineers have been able to develop low-drag automotive designs through detail and shape optimization. In the past, this would require extensive wind tunnel tests to examine the effects of each modification on vehicle performance. Today, such effects can be assessed and analyzed using Computational Fluid Dynamics (CFD).

CFD is a logical choice for a design tool because it provides flexibility and reduces the time and cost associated with iterative wind tunnel testing. However, its usefulness and applicability is predicated on its ability to

simulate and predict the essential physics of the flow field. This is especially true for the rear end of an automobile where low pressures induced by the separated flow can have significant effects on pressure drag. Carr [1]<sup>1</sup> estimated that rear-end drag accounts for 50% of the total body drag on a typical notchback configuration. Thus, a code's ability or inability to simulate the flow field in this region can have a significant effect on drag prediction and emphasizes the need for detailed comparisons with experimental data. Undoubtedly, immense databases have been generated through years of automotive testing, but it is uncertain whether such databases have the appropriate data, documentation, and accuracy to validate CFD flow solvers. The literature contains many qualitative descriptions of the flow over notchback rear ends and surface pressure data are readily available; however, the amount of quantitative flow-field information is limited.

## FLOW SEPARATION ON A NOTCHBACK REAR END

The flow structure on a notchback rear end is characterized by quasi-two-dimensional and three-dimensional separation [2], reverse flow, and high turbulence levels. Massive flow separation typically occurs along the trailing edges of the roof, decklid and along the C-pillar. Much of the complexity associated with this flow field is due to the proximity of the separated flows and their inherent interaction. The next three sections describe the regions of separated flow and discuss factors that influence their formation and characteristics.

**ROOF SEPARATION** – In the center plane, quasi-two-dimensional separation begins when the roof boundary layer detaches as it approaches the roof trailing edge and encounters an adverse pressure gradient. The detachment location depends on the roof trailing-edge radius and the state of the boundary layer. If the trailing edge is sharp, flow detachment occurs at the edge regardless of the state of the boundary layer. If the trailing edge is rounded, the state of the boundary layer

---

1. Number in brackets refer to the references at the end of the paper.

determines how far the flow remains attached around the edge radius.

Detachment results in the formation of a shear layer that extends downstream into the wake or reattaches on the decklid. Reattachment depends on decklid length ( $l$ ), height ( $d$ ), and backlight angle ( $\alpha$ ) shown in Figure 1, as well as the amount of downwash induced in the center plane. Carr [3] recorded surface patterns for different combinations of  $\alpha$  and  $l$  and observed that reattachment occurred when  $\beta \leq 35$  degrees. Carr defined  $\beta$ , also shown in Figure 1, as the declination angle or the minimum angle that the separated flow from the roof trailing edge must follow to reattach on the decklid. Nouzawa, et. al. [4] performed a similar investigation using different combinations of  $\alpha$ ,  $l$ , and  $d$ , and found a critical angle,  $\beta = 25$  degrees, below which the flow would reattach and above which, the flow would remain detached. A comparison between the notchback flow field and the flow over a backward-facing step by Hucho [5] cites work by Dilgen that predicts reattachment at a location three to five step-heights downstream of the detachment point. Applying this to a notchback decklid, which is typically two step-heights in length, Hucho concluded that the flow will not reattach unless acted upon by side vortices. These side vortices, which will be discussed later, impart downward momentum to the center-plane flow.

After reattachment on the decklid, a separation bubble is formed as the flow bifurcates and moves upstream and downstream. Carr [3] deduced that the flow traveling upstream and the circulatory patterns on each side of the decklid, shown in Figure 2, indicate a transverse vortex that generates downwash and substantial lift on the car rear end. The open literature contains few quantitative measurements to support the existence of such a vortex but a recirculating flow pattern has been predicted computationally by Tatchell [6], Hutchings and Pien [7], Kataoka, et. al. [8], and Hajiloo, et. al. [9]. Computations and experiments by Nouzawa, et. al. [10] show the presence of a separation bubble when  $\beta \leq 25$  degrees. They also found that when  $\beta = 25$  degrees, the recirculation in the bubble forms the arch vortex shown in Figure 3. Nouzawa, et. al. suggest that this vortex "bends" the detached flow from the roof and contributes to the circulation of the trailing vortex system.

**DECKLID SEPARATION** – Although flow separation at the decklid trailing edge was not investigated as part of this work, a brief description is warranted to provide a complete picture of the flow field. Like the separation at the roof trailing edge, quasi-two-dimensional flow separation initiates along the decklid trailing edge and culminates when flow from above and below the car merge to form a separation bubble behind the base. Visualization studies by Ahmed and Baumert [11] have shown that the bubble's internal structure consists of two re-circulating flow patterns. Some computational investigations [7,8,9,12,13] have predicted similar flow patterns and have shown the bubble size and structure to be dependent on the turbulence model and grid spacing.

Surveys by Williams, et. al. [12,13] show the lateral and vertical extent of the separation bubble but the seven-hole probe used in the experiment could not measure the reverse flow.

Downstream of the base separation bubble, two streamwise vortices are formed which dominate the far-wake. The location and characteristics of these vortices have been documented by several researchers using total pressure, multi-hole, and hot-wire probes [9,11,12,13,14]. Their results show single and multiple vortices that move toward the ground and away from the center plane with increasing downstream distance.

**C-PILLAR SEPARATION** – Three-dimensional separation on the C-pillar and the resulting vortex formation on the notchback rear end are dependent on the backlight angle and aspect ratio [5]. Morel [15] investigated the effect of base slant on the drag of an axisymmetric body and found that vortices were only formed when the base slant angle was less than 43 degrees. Figure 4 presents a separation pattern deduced by Ahmed, et. al. [16] that shows a C-pillar vortex and a vortex pair in the base separation bubble on a vehicle-like body with a slanted base ( $\alpha \leq 25$  degrees). Hucho [5] suggests that the higher aspect ratio of the backlight on notchbacks produces a weaker vortex. This may explain why the C-pillar vortex is not as apparent in wake measurements by numerous researchers [11,12,13,14]. Although some computational investigations [9,12,13] have predicted several vortex pairs in the near-wake of notchback configurations, it cannot be determined which, if any, may be C-pillar vortices. Flow patterns presented by Carr [3] and Nouzawa, et. al. [10] imply that the C-pillar separation may not form streamwise vortices like on a fastback rear end but may instead be part of the transverse vortex behind the backlight.

The significance of the C-pillar vortex is the downwash it induces in the center plane, which pulls the detached flow from the roof toward the decklid [5]. This is most notable on fastback rear ends where for a certain range of  $\alpha$ 's, the downwash can force the flow to remain attached [17] or change the detachment location [18]. The effect is less pronounced on a notchback rear end where, as previously stated, the larger aspect ratio of the backlight can result in a weaker downwash. Nevertheless, Carr [3] did note the influence of a strong downwash on flow reattachment and observed that it also delayed flow detachment along the decklid trailing edge.

## EXPERIMENTAL SETUP

**TEST FACILITY** – The NASA-Langley Basic Aerodynamics Research Tunnel (BART) is a flow-diagnostic facility that specializes in the acquisition of detailed data for the development and validation of CFD models and techniques. Its flexibility and advanced measurement capabilities are often utilized to investigate the fundamental characteristics of complex flow fields about various vehicle configurations.

The BART, shown in Figures 5 and 6, is a subsonic, open-return wind tunnel with a closed test section 0.711 meters high, 1.016 meters wide and 3.048 meters long. During operation, air is drawn into the tunnel inlet under atmospheric conditions by a 9 blade-11 stator fan. The fan is powered by an 125 horsepower, alternating current motor coupled to a magnetic clutch. Air passes through a honeycomb, four anti-turbulence screens, and an 11:1 contraction before entering the test section. The maximum velocity at the test section entrance is 56 m/s, which corresponds to a unit Reynolds Number ( $Re/m$ ) of 3.64 million. The turbulence intensity varies from 0.03% at 15 m/s to 0.09% at tunnel maximum velocity. Additional information about the BART can be found in [19, 20, 21].

**MODEL** – The car used in this investigation was a 16% scale, aluminum model of the Ford C1 configuration. Figure 7 provides frontal, planform, and elevation views of the model with dimensions. Additional details about the geometry can be found in [12,13,21]. The car was mounted on four, airfoil-shape struts attached to a stationary ground plane. This configuration provided flexibility for model placement, permitted yaw adjustments, and elevated the model for better access when using the BART Laser Velocimeter System (LVS). The ground plane was constructed from aluminum and measured 2.536 meters long and 0.914 meters wide. Based on projected frontal area, the model, airfoil struts, and ground plane produce a solid blockage ratio of 0.0738. The complete test configuration is shown in Figure 8 and described in [21].

Use of a ground plane and the associated effect on the empty tunnel pressure gradient typically requires the test section to be re-calibrated. In this case, the entire test section could not be calibrated so a pitot-static probe was used to measure the empty tunnel dynamic pressure at the model reference plane shown in Figure 9. The ratio of the dynamic pressures at the model and tunnel reference planes established a correction factor of 1.17 used to set the test conditions. Table 1 shows the conditions set at the tunnel reference and the corresponding conditions at the model reference.

Table 1. Test conditions at tunnel and model reference locations.

	Tunnel Reference	Model Reference
Dynamic Pressure, $q$	1.64 kPa	1.92 kPa
Freestream Velocity, $U_\infty$	51.7 m/s	55.92 m/s
Reynolds No. based on model length ( $L = 0.825$ m)	$3.36 \times 10^6$	$3.64 \times 10^6$

## MEASUREMENT TECHNIQUES

**Surface Flow Visualization** – Prior to making off-body flow-field measurements, surface flow visualization was performed to identify separation and attachment lines, nodes, recirculating flow regions, and other surface flow features. Surface flow patterns along the model upper surface were visualized using a mixture comprised of titanium dioxide ( $TiO_2$ ) and kerosene. The entire process was recorded on video tape and the final flow pattern was documented using a film-based camera.

**Surface Pressure Measurements** – Surface pressures were measured using ninety-three orifices drilled in the model surface. Sixty-seven orifices were distributed along the centerline and thirteen orifices were distributed around each A-pillar. Pressure coefficients were calculated using the measured pressures ( $p$ ), total pressure ( $p_t$ ), static pressure ( $p_\infty$ ), and the following equation:

$$C_p = \frac{p - p_\infty}{p_t - p_\infty} \quad (1)$$

The estimated uncertainty in  $C_p$  is  $\pm 0.029$ .

**Boundary Layer Measurements** – Boundary layer surveys were conducted along the roof centerline at  $x_m/L = 0.034$  and  $x_m/L = 0.154$ , where  $x_m$  is the distance from the model reference location shown in Figure 9 and  $L$  is the length of the model, 0.825 meters. In each survey, the boundary layer probe was traversed from the roof surface to a height 2.54 cm above the surface. The total pressure from the probe and the static pressure from a surface orifice in the vicinity of the probe were acquired at 46 measurement points and converted to velocities. The estimated uncertainty in probe position and calculated velocity were  $\pm 0.010$  cm and  $\pm 0.053$  m/s, respectively. The state of the boundary layer was evaluated by comparing the profiles to the Law of the Wall.

**Flow-Field Measurements** – The vortical flow and boundary layer separation associated with this particular automobile configuration required the use of a technique capable of measuring reverse flow and large shear gradients. As such, a laser velocimeter was chosen to acquire the flow-field information. The BART LVS is a three-color, orthogonal, cross-fringed system. Figure 10 provides a schematic of the system components and orientation. A six-watt, Argon-ion laser produced a multi-line laser beam from which the 514.5 nm, 496.5 nm, and 476.5 nm lines or wavelengths were used to measure the transverse, vertical, and streamwise velocity components, respectively. Monodispersed polystyrene microspheres with a diameter of 0.9 microns served as the light scattering media. A complete description of the system, including its components and previous applications, can be found in [21,22,23,24].

## RESULTS AND DISCUSSION

**SURFACE FLOW** – Figures 11, 12, and 13 present the rear-end surface flow pattern. The line along the centerline and the short lines perpendicular to it are not part of the surface flow pattern but were produced by the LVS during system alignment. In Figures 11 and 12, the surface streamlines on the side panel and side glass are divided by a line of separation formed upstream at the base of the windshield. Fluid from the side panel detaches at the base except for a small portion that flows up and over the outboard edge of the decklid. Similarly, fluid from the side glass detaches along the C-pillar except for a small portion that flows onto the roof. On the roof, this fluid converges to a line of separation associated with the A-pillar vortex.

Figure 13 shows the complicated interaction of fluid from the roof and sides of the car on the decklid. In the center plane, fluid detaches at the roof trailing edge (point B5) but its attachment point on the decklid is not readily apparent. Surface streamlines in the vicinity of C6 indicate flow toward the center plane and subsequent bifurcation at saddle point C5. Fluid moving downstream converges in the center plane before it accelerates around the decklid trailing edge and detaches to form the base separation bubble. Fluid moving upstream also converges to the center plane but appears to be highly influenced by spiral nodes located near the C-pillars (points H5). At the juncture between the backlight and decklid, fluid detaches from the surface (point D5) as it encounters an adverse pressure gradient and reattaches on the backlight (point E5). Some of the reattaching fluid flows downward and forms a small vortex in the juncture between the backlight and the decklid (points D5 and E5). The rest of the fluid moves upward, bifurcates at a saddle point (point F5), and moves outboard toward the C-pillars. Near the C-pillars, the flow bifurcates again and travels around the peculiar patterns labeled G5. These are believed to be associated with the C-pillar vortices but their orientation and other details are difficult to discern. The overall surface pattern is comparable to the surface pattern shown in [12] for a 0.5-scale C1 model with the exception of two additional saddle points outboard of the attachment lines. Although some details are obscured by the effects of flow unsteadiness on the TiO<sub>2</sub>, saddle points were only detected on the centerline of this configuration.

The spiral nodes behind the backlight resemble the patterns shown in Figures 2 and 3, however, off-body measurements provide no evidence of a transverse or arch vortex. It will be shown later that these are the origins of “decklid” vortices that form on the surface and dominate the flow field over the decklid. During the visualization study, the spiral nodes exhibited strong, dynamic characteristics as they randomly ejected the TiO<sub>2</sub> mixture over the decklid and onto the backlight. Fluid that was splashed onto the backlight eventually flowed downward due to gravity and rejoined the spiral nodes.

**SURFACE PRESSURES** – The measured pressure distribution along the car centerline is presented in Figure 14 and shows the typical pressure loss and recovery associated with notchback configurations. The highest pressure on the decklid occurs at  $x_m/L = 0.437$ , which is in close proximity to the saddle point described in the previous section. This location also agrees with results from the 0.5-scale model [9] and indicates that the flow features may scale with model size.

**BOUNDARY LAYER** – Boundary layer profiles measured in the roof center plane are compared in Figure 15. Differences in the profiles are attributed to their relative locations with respect to the centerline pressure gradient. At  $x_m/L = 0.034$  the boundary layer is recovering from flow acceleration around the roof leading edge, while at  $x_m/L = 0.154$ , the boundary layer begins to respond to higher pressures on the rear of the car.

In order to evaluate the state of the boundary layer, the data were converted to wall variables using the following equations:

$$u^+ = \frac{U}{U_e} \sqrt{\frac{2}{C_f}} \quad (2)$$

and

$$y^+ = \frac{U_e y}{\nu} \sqrt{\frac{C_f}{2}} \quad (3)$$

Here,  $U$  is the mean velocity,  $U_e$  is the velocity at the edge of the boundary layer,  $C_f$  is the skin friction coefficient estimated using the Clauser Method, and  $\nu$  is the kinematic viscosity. The converted data were plotted against Spalding's Formula for the Law of the Wall,

$$y^+ = u^+ + e^{-\kappa B} \left[ e^{\kappa u^+} - 1 - \kappa u^+ - \frac{(\kappa u^+)^2}{2} - \frac{(\kappa u^+)^3}{6} \right] \quad (4)$$

where  $\kappa$  is the von Kármán constant, ( $= 0.41$ ) and  $B$  is the wall-law intercept constant ( $= 5.0$ ). Figure 16 shows the overlap between the measured profile and the theoretical curve in the logarithmic region. This overlap indicates that the boundary layer on the roof centerline is turbulent prior to its detachment at the roof trailing edge.

### OFF-BODY FLOW FIELD

**Center-Plane Flow** – The LVS was used to measure profiles every 1.22 cm between  $x_m/L = 0.236$  and  $x_m/L = 0.502$ . In each profile, the sample volume was placed at  $z/H = 1.107$  and traversed downward to the car surface in 0.254 cm increments.  $z$  is the vertical distance away from the ground plane and  $H$  is the distance between the ground plane and the top of the car, nominally 23.698 cm. Close to the car surface, the signal-to-noise ratio was too low to properly resolve the velocities. As such, data

were only obtainable to within 0.508 - 0.762 cm of the surface. The estimated uncertainty in the mean velocities and turbulence intensities is less than 1.5 percent and 1.0 percent of the freestream velocity, respectively.

Figure 17 presents selected streamwise and vertical velocities along with a graphic depicting the measurement locations behind the backlight. The dashed line in Figure 17c denotes the location in each profile at which the streamwise turbulence intensity achieves its maximum value. This line approximates the centerline of the shear layer [25,26] and will be used when describing the profiles. Figure 17a shows that  $U/U_\infty$  is constant above the shear layer in a given profile but decreases with downstream distance due to flow deceleration. Below the shear layer, the sign of  $U/U_\infty$  changes from positive to negative between  $x_m/L = 0.399$  and  $x_m/L = 0.430$ .  $W/U_\infty$  exhibits a similar trend in Figure 17b as it changes from negative above the shear layer to positive near the surface. Such changes in flow direction are consistent with the saddle point identified in the decklid surface flow pattern.

The vector plot in Figure 18 and the streamline plot in Figure 19 reveal the time-averaged flow structure in the center plane. The streamline pattern is quite similar to computational results on the 0.5 scale model [9,12,13] and shows that the shear layer from the roof trailing edge does not reattach in the center plane of the decklid. The figures also show no evidence of a transverse vortex behind the backlight where reverse flow occurs. The next three sections will discuss these flow-field features in detail.

**Detachment** – The detachment location was determined from the surface flow visualization results, centerline pressure distribution, and flow-field measurements. In Figure 13, detachment is indicated by the accumulation of fluid along the roof trailing edge (B5). Using the pressure orifices as reference points, detachment was estimated to occur over a region between  $x_m/L = 0.286$  and  $x_m/L = 0.293$ . Correspondingly, the centerline  $C_p$ 's show a 0.216 change between the two orifices near this location (Figure 14). To obtain quantitative information about the detachment region, nine additional velocity surveys were conducted in the center plane from  $x_m/L = 0.273$  to  $x_m/L = 0.299$ . Unlike the other center-plane surveys, these nine surveys were acquired with the LVS in "coincidence" mode. As such, the data include mean velocities, turbulence intensities and turbulent normal and shear stresses.

Figure 20 compares selected velocity profiles and turbulence quantities measured near the detachment location at  $x_m/L = 0.284$ , 0.288, 0.292, and 0.294. In general, the profiles are similar over the range from  $z/H = 0.986$  to  $z/H = 1.111$  but below  $z/H = 0.986$ , the two upstream profiles begin to differ from the two downstream profiles. Based on the surface flow results and the centerline pressure distribution, these profile groupings probably represent pre- and post-detachment

flows and suggest that detachment occurs between  $x_m/L = 0.288$  and  $x_m/L = 0.292$ .

**Shear Layer** – In the center plane, the upward pointing vectors and streamline pattern in Figures 18 and 19 provide evidence that the shear layer does not attach to the decklid but extends downstream into the wake. This result is surprising because most models of the flow field on a notchback rear-end show flow detachment from the roof and attachment on the decklid. According to the criteria developed by Carr [3] and the calculated declination angle for this model (approximately 21 degrees), the shear layer should reattach. Figure 21 shows that the shear layer passes through a small angle and curves away from the surface. Reattachment on Carr's model occurred "under the action of a strong downwash apparently caused by a transverse vortex system rather than the edge vortices." Hucho [5] suggests that the side vortices are responsible for flow reattachment. Both concepts imply that downwash is required for reattachment but the vector plot in Figure 18 shows that none exists. The vectors do show an upflow at  $x_m/L = 0.430$  that merges with the outer flow. From the surface flow pattern in Figure 13, it is believed that this upflow is created by the convergence of fluid streams or inflow from the sides of the decklid in the center plane. As the two streams meet, the pressure increases and forces fluid away from the surface with sufficient momentum to deflect the outer flow. Williams, et. al. [13] describe an "upswelling of low energy air" in the center of the decklid due to inflow but did not comment on its interaction with the shear layer. Undoubtedly, additional measurements are necessary to explain this interaction.

**Reverse Flow** – Velocity profiles in Figure 17a show significant reverse flow below the shear layer. The maximum reverse flow velocity is 25 percent of the freestream velocity, which is higher than that associated with backward-facing steps [27]. The reverse flow also has a large vertical component. Profiles of  $W/U_\infty$  show upward velocities between 5 and 20 percent of the freestream velocity. Handford and Bradshaw [28] measured large vertical velocities behind surface-mounted semi-bluff bodies and attributed them to the pressure field. In this case, the pressure field is associated with the inflow and saddle point in the center of the decklid.

It should also be noted that measurements in this region show no evidence of a transverse vortex as postulated by other researchers. This is reflected in the center-plane vector field, Figure 18, as well as in the transverse vorticity,  $\omega_y$ , calculated from the equation,

$$\omega_y = \left( \frac{\partial u}{\partial z} - \frac{\partial w}{\partial x} \right) \quad (5)$$

Figure 22 shows that all of the transverse vorticity is concentrated in the shear layer and not behind the backlight where a transverse vortex would exist.

**Cross Flow** – A velocity survey was also performed in a single, transverse plane at  $x_m/L = 0.340$  to examine the cross-flow characteristics of the separated region. The survey was performed using the LVS and consisted of 150 points distributed between  $y/(b/2) = 0.083$  and  $y/(b/2) = -1.181$  and between  $z/H = 0.801$  and  $z/H = 1.029$ . Here, the transverse distances from the center plane of the model ( $y$ ), have been normalized by half of the model width. Measurements were made every 1.219 cm. in the transverse direction and every 0.610 cm. in the vertical direction.

Figures 23, 24, and 25 present contour plots of mean velocities in the survey plane normalized by the freestream velocity. Contours of  $U/U_\infty$  in Figure 23 show an arch-shaped shear layer and the extent of the reverse flow in the transverse direction. The distortion in the upper left corner probably results from strong inflow and downwash shown in Figures 24 and 25, respectively. Positive and negative values of  $V/U_\infty$  and  $W/U_\infty$  below the shear layer indicate the presence of rotational flow.

Transverse and vertical velocity components were used to produce the vector field shown in Figure 26. The vector plot shows strong inflow from the sides of the car and the presence of rotational flow between  $y/(b/2) = 0.00$  and  $y/(b/2) = -0.604$ . Figure 27 shows a contour plot of the streamwise vorticity in the survey plane calculated using the equation

$$\omega_x = \left( \frac{\partial v}{\partial z} - \frac{\partial w}{\partial y} \right) \quad (6)$$

The figure reveals the existence of three vortices centered at  $y/(b/2) = -0.375$ ,  $z/H = 0.946$ ;  $y/(b/2) = -0.454$ ,  $z/H = 0.874$ ; and  $y/(b/2) = -0.197$ ,  $z/H = 0.834$ . The skewed lower vortex (vortex A), has a counter-clockwise rotation and is consistent with the rotation of the spiral nodes at point H5 and the flow pattern on the backlight in the surface flow images (Figure 13). Nouzawa, et. al. [10] identified a vortex with counter-clockwise rotation at the height of the backlight in wake surveys but did not comment on its source. The middle vortex (vortex B) could be the C-pillar vortex and may emanate from the patterns identified at points G5 in Figure 13. The upper vortex (vortex C) has a counter-clockwise rotation and its size and location suggest that it may be the A-pillar vortex. Although additional transverse surveys are necessary to properly document the development and trajectory of these vortices, Figure 28 presents a possible trajectory for the A-pillar vortex inferred from the surface flow pattern and the location of vortex C in the transverse plane.

**FLOW TOPOLOGY** – Figure 29 presents the overall flow structure deduced from the data. The figure highlights features that influence the transport of fluid to and over the decklid. These include vortices formed on the front of the car, vortices formed on the backlight and decklid, and

inflow from the sides of the car. The labels in the figure correspond to those used in Figure 13.

**Upstream Vortices** – The figure shows the trajectory of the A-pillar vortices and their sense of rotation as they extend downstream over the roof. Figure 27 confirms that the A-pillar vortex is still intact at  $x_m/L = 0.340$  but it is uncertain what happens as it continues downstream. This is denoted by the dotted lines.

**Backlight and Decklid Vortices** – Part of the flow that detaches at the C-pillar and the rear corner of the roof forms the recirculating patterns at G5. The surface pattern in this region was extremely complex but it is believed that these are the origins of C-pillar vortices described previously. Closer to the decklid, fluid flows around the base of the C-pillar and forms “decklid” vortices behind the backlight (H5). As opposed to extending downstream, the inflow from the sides of car forces these vortices toward the center plane where they interact. The dynamics of their interaction are still unclear but they appear to induce reverse flow and an upwash between point C5 and the backlight. On the decklid centerline, the reverse flow travels up the backlight and bifurcates at the saddle point F5. From there, the fluid flows outboard where it joins the C-pillar or decklid vortices.

**Inflow** – After detachment, the shear layer on each side of the roof centerline merges with the decklid vortices. The decklid vortices transport this fluid down to the surface where it impinges in the vicinity of C6. Part of the fluid travels upstream toward the backlight and part of it increases the inflow toward the center plane. In the center plane, the inflow converges to form a saddle point at C5 where the fluid is deflected upstream, downstream, and upward, away from the decklid. Upstream-moving fluid joins the other reverse flow, whereas downstream-moving fluid eventually detaches at the decklid trailing edge and forms the base separation bubble. Upward-moving fluid imparts vertical and streamwise momentum to the center plane flow, which prevents it from attaching on the decklid.

## CONCLUSION

An experimental investigation of the flow over a notchback automobile configuration has been conducted to provide quantitative information about the flow field behind the backlight. Results obtained in this investigation include surface flow patterns, boundary-layer profiles, surface pressures, mean velocities and turbulence intensities for one Reynolds number. Off-body data were acquired in the center plane and a single transverse plane behind the backlight. This research gives insight into the evolution and time-average structure of the flow separation and provides a detailed dataset for comparison with computer simulations.

The flow field behind the backlight of this configuration was found to contain many unique features that differ from the generally accepted models for the flow over a notchback rear end. First, the separation process is not quasi-two-dimensional as it is often depicted. Instead, the flow separation is dominated by two "decklid" vortices that form behind the backlight and extend toward the center of the decklid. These vortices entrain the shear layer formed on either side of the roof centerline and induce reverse flow over the decklid. Secondly, the shear layer formed in the center plane at the roof trailing edge does not attach on the decklid but extends downstream. Upflow induced by the decklid vortices and the convergence of fluid from the sides of the decklid appears to deflect the shear layer away from the surface, thereby preventing attachment. Lastly, the notchback geometry used in this investigation is comparable to a backward-facing step but does not produce a transverse vortex in the juncture between the backlight and the decklid.

## ACKNOWLEDGMENTS

The author wishes to thank Anthony Washburn, William Sellers, and Bobby Gaddy of the NASA Langley Research Center for their assistance in the completion of this investigation; Dave Rollins and Hayward Glaspel of the NASA Langley Research Center for fabrication of the model; Jack Williams of the Ford Motor Corporation for providing the geometry and impetus for this work; and James Hackett and Scott Thompson of Lockheed-Martin for sharing their knowledge and expertise.

## REFERENCES

1. Carr, G. W., Potential for Aerodynamic Drag Reduction in Car Design, *International Journal of Vehicle Design*, Special Publication SP3, 1983, pp. 44-56.
2. Hucho, W-H., The Aerodynamic Drag of Cars - Current Understanding, Unresolved Problems, and Future Prospects, *Aerodynamic Drag Mechanisms of Bluff Bodies and Road Vehicles*, edited by G. Sovran, T. Morel, and W. T. Mason, Jr., Plenum Press, New York, 1978, pp. 7-44.
3. Carr, G. W., *Influence of Rear Body Shape on the Aerodynamic Characteristics of Saloon Cars*, MIRA Report 1974/2, 1974.
4. Nouzawa, T., Hiasa, K., Nakamura, T., Kawamoto, A., and Sato, H., Unsteady-Wake Analysis of the Aerodynamic Drag of a Notchback Model with Critical Afterbody, *Vehicle Aerodynamics: Wake Flows, Computational Fluid Dynamics, and Aerodynamic Testing*, SP-908, SAE, Pennsylvania, pp. 1-12.
5. Hucho, W. H., Aerodynamic Drag of Passenger Cars, *Aerodynamics of Road Vehicles*, edited by W. H. Hucho, SAE, Pennsylvania, 1989, pp. 131-238.
6. Tatchell, D. G., *Application of the PHOENICS Code to External Aerodynamics of Road Vehicles*, CHAM tr/73, September 1981.
7. Hutchings, B. J. and Pien, W., Computation of Three-Dimensional Vehicle Aerodynamics Using FLUENT/BFC, *Proceedings of the Second International Conference on Supercomputing Applications in the Automotive Industry*, 1988, pp. 233-255.
8. Kataoka, T., China, H., Nakagawa, K., Yanagimoto, K., and Yoshida, M., Numerical Simulation of Road Vehicle Aerodynamics and Effect of Aerodynamic Devices, *Vehicle Aerodynamics: Recent Progress*, SP-855, SAE, Pennsylvania, 1991, pp. 151-163.
9. Hajiloo, A., Williams, J., Hackett, J. E., and Thompson, S. A., Limited Mesh Refinement Study of the Aerodynamic Flow Around a Car-Like Shape: Computational Versus Experimental Fluid Dynamics, *Vehicle Aerodynamics: Wind Tunnels, CFD, Aeroacoustics, and Ground Transportation Systems*, SP-1145, SAE, Pennsylvania, 1996, pp. 63-73.
10. Nouzawa, T., Haruna, S., Hiasa, K., Nakamura, T., and Sato, H., Analysis of the Wake Pattern for Reducing Aerodynamic Drag of Notchback Models, *SAE 1990 Transactions - Journal of Passenger Cars*, Sec. 6, Vol. 99, 1990, pp. 486-494.
11. Ahmed, S. R. and Baumert, W., The Structure of Wake Flow Behind Road Vehicles, *Aerodynamics of Transportation - ASME-CSME Conference*, edited by T. Morel and C. Dalton, SAE, New York, 1979, pp. 93-103.
12. Williams, J., Quinlan, W. J. , Hackett, J. E., Thompson, S. A., Marinaccio, T., and Robertson, A., *A Calibration Study of CFD for Automotive Shapes and  $C_D$* , *Analysis of Vehicle Aerodynamics*, SAE SP-1036, SAE, Pennsylvania, 1994, pp. 1-20.
13. Williams, J., Quinlan, W. J. , Hackett, J. E., Thompson, S. A., Marinaccio, T., and Robertson, A., *A CFD Calibration Study for Automotive Shapes*, AIAA 94-2607, 1994.
14. Cogotti, A., *Car-Wake Imaging Using a Seven-Hole Probe*, SAE Paper No. 860214, 1986.
15. Morel, T., Effect of Base Slant on Flow in the Near Wake of an Axisymmetric Cylinder, *Aeronautical Quarterly*, Vol. 31, May 1980, pp. 132-147.
16. Ahmed, S. R., Ramm, G., and Faltn, G., Some Salient Features of the Time-Average Ground Vehicle Wake, *Automobile Aerodynamics: Wakes, Wind Effect, Vehicle Development*, SP-569, SAE, Pennsylvania, 1984.
17. Ahmed, S. R., Influence of Base Slant on the Wake Structure and Drag of Road Vehicles, *ASME Journal of Fluids Engineering*, Vol. 105, 1983, pp. 429-434.
18. Janssen, L. J. and Hucho, W. H., Aerodynamische Formoptimierung der Typen VW Golf and VW Scirocco, *Proceedings of Kolloquium ueber Industrieaerodynamik*, Part 3, 1974, pp. 49-70.
19. Sellers, W. L., III and Kjelgaard, S. O.: *The Basic Aerodynamics Research Tunnel - A Facility Dedicated to Code Validation*, AIAA-88-1997, May, 1988.
20. Washburn, A. E.: The Effect of Freestream Turbulence on the Vortical Flow over a Delta Wing, Master of Science Thesis, George Washington University, December, 1990

21. Jenkins, L. N.: An Experimental Investigation of the Flow Over a Notchback Automobile Configuration, Master of Science Thesis, George Washington University, January, 1999.
22. Meyers, J. F. and Hepner, T. E., Measurement of Leading Edge Vortices From a Delta Wing Using a Three Component Laser Velocimeter, *A Collection of Technical Papers – AIAA 15<sup>th</sup> Aerodynamic Testing Conference*, May 1988, pp. 223-233.
23. Kjelgaard, S. O. and Sellers III, W. L., *Detailed Flow-Field Measurements Over a 75° Swept Delta Wing*, NASA TP 2997, October 1990.
24. Sellers III, W. L., Meyers, J. F., and Hepner, T. E., *LDV Surveys Over a Fighter Model at Moderate to High Angles of Attack*, SAE 88-1448, October 1988.
25. Kiya, M. and Sasaki, K., Structure of a Turbulent Separation Bubble, *Journal of Fluid Mechanics*, Vol. 137, 1983, pp. 83-113.
26. Ruderich, R. and Fernholz, H. H., An Experimental Investigation of a Turbulent Shear Flow with Separation, Reverse Flow, and Reattachment, *Journal of Fluid Mechanics*, Vol. 163, 1986, pp. 283-322.
27. Eaton, J. K. and Johnston, J. P., A Review of Research on Subsonic Turbulent Flow Reattachment, *AIAA Journal*, Vol. 19, No. 9, September 1981, pp. 1093-1100.
28. Handford, P. M. and Bradshaw, P., Flow Over Surface-Mounted Semi-Bluff Bodies, *Proceedings of the Symposium on Numerical and Physical Aspects of Aerodynamic Flows*, 1985, pp. 7-13 to 7-21.

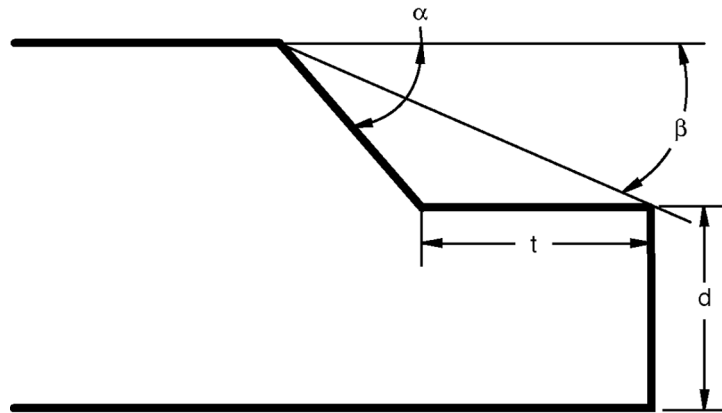


Figure 1. Notchback rear-end parameters.

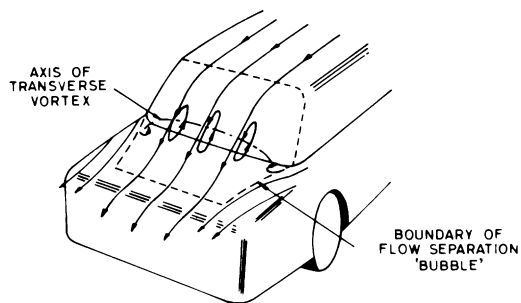


Figure 2. Transverse vortex (Carr [3]).

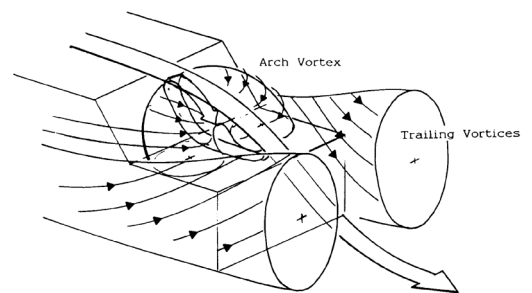


Figure 3. Arch-vortex (Nouzawa, et. al. [10]).

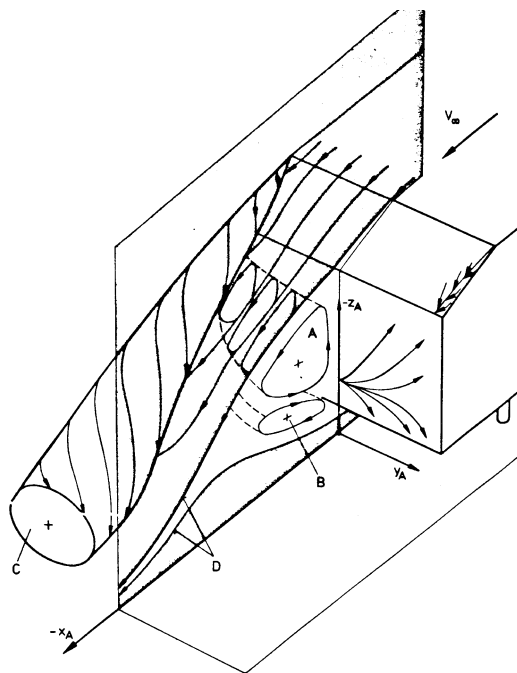


Figure 4. Rear-end flow pattern on Ahmed's "vehicle-like" body (Ahmed, et. al. [17]).



Figure 5. The NASA Langley Basic Aerodynamics Research Tunnel (BART).

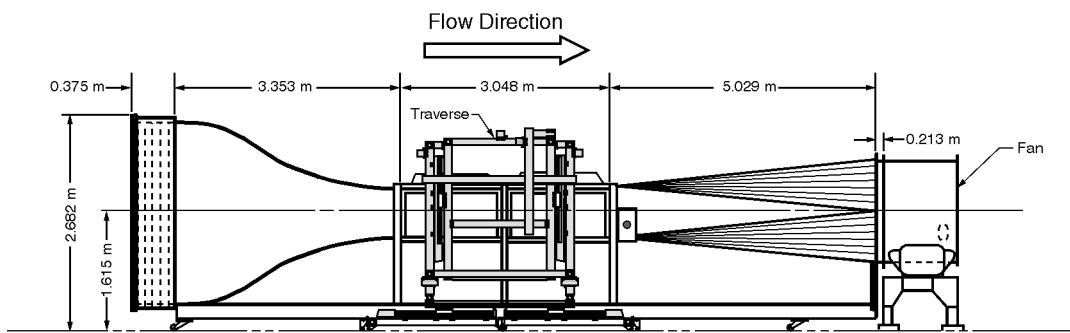


Figure 6. Elevation view of the BART.

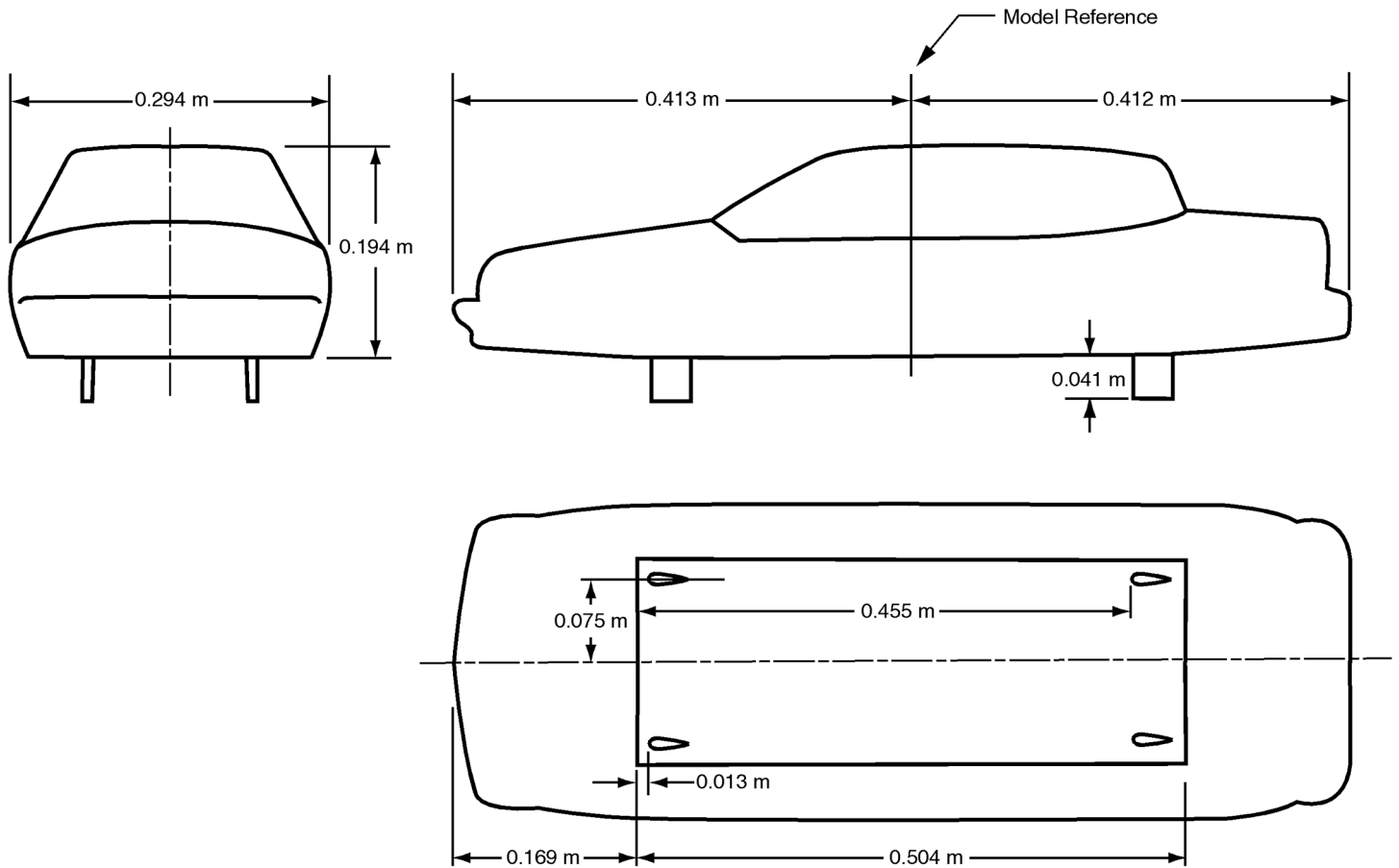


Figure 7. Model dimensions and airfoil strut attachment locations.

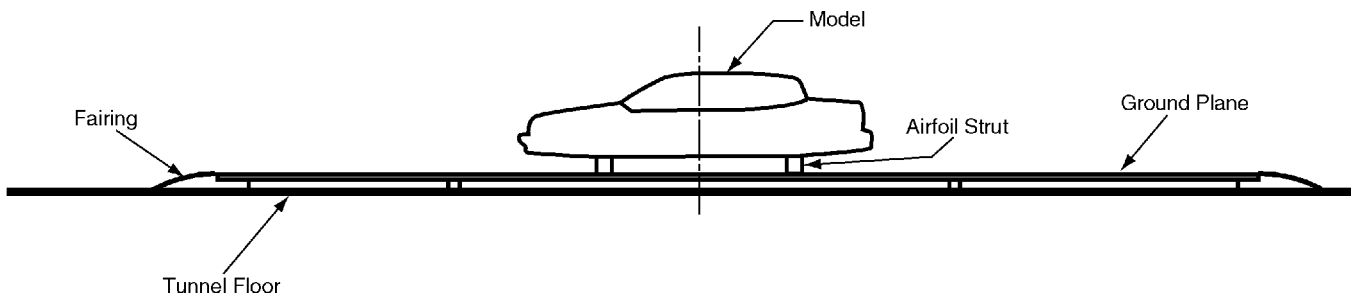


Figure 8. Assembly drawing of the experimental setup.

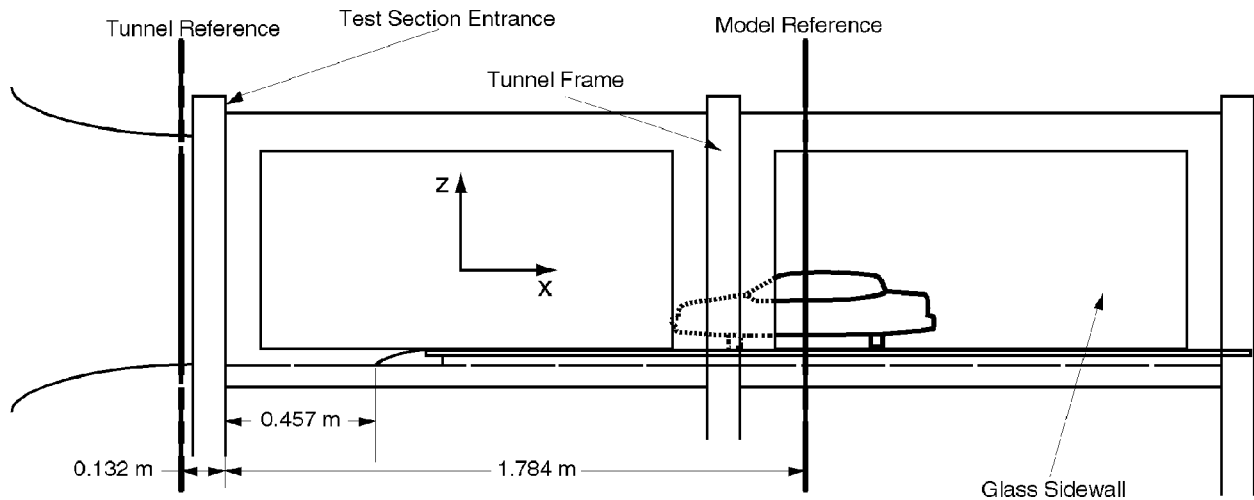


Figure 9. Installation schematic and reference locations (not drawn to scale).

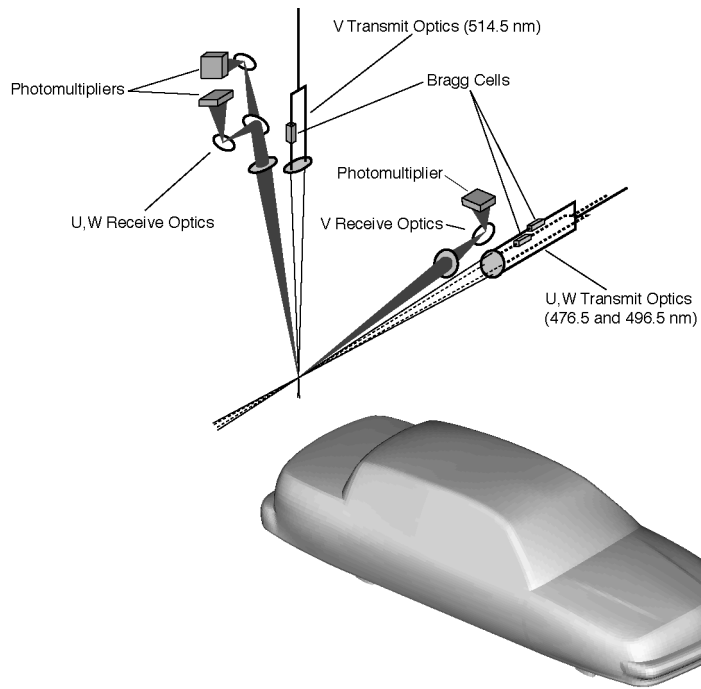


Figure 10. Schematic of the LVS setup.



Figure 11. Rear-end surface flow pattern - Passenger's Side View.

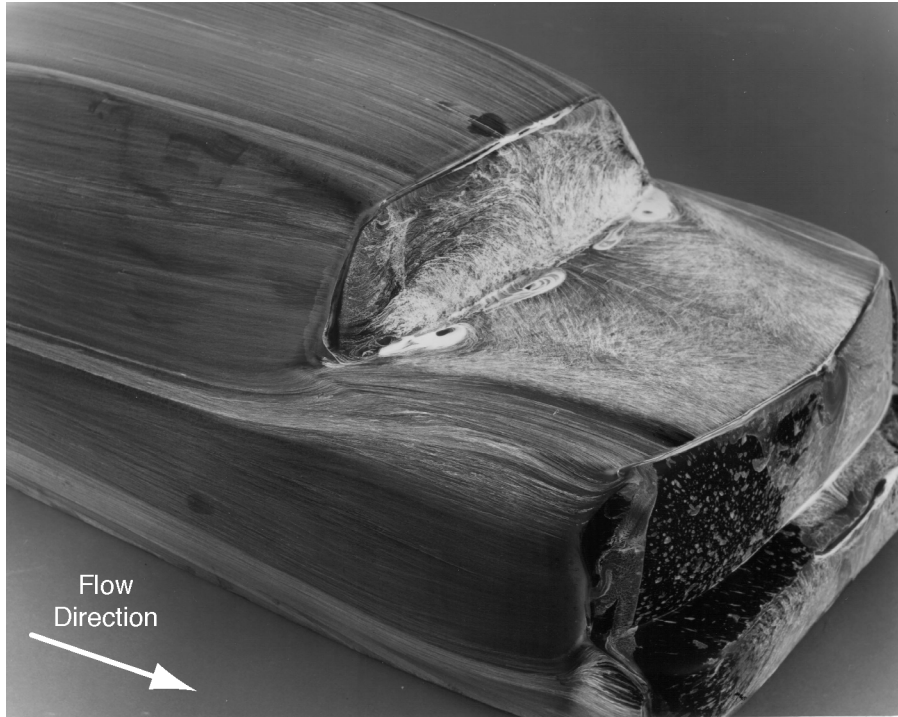


Figure 12. Rear-end surface flow pattern - Driver's Side View.

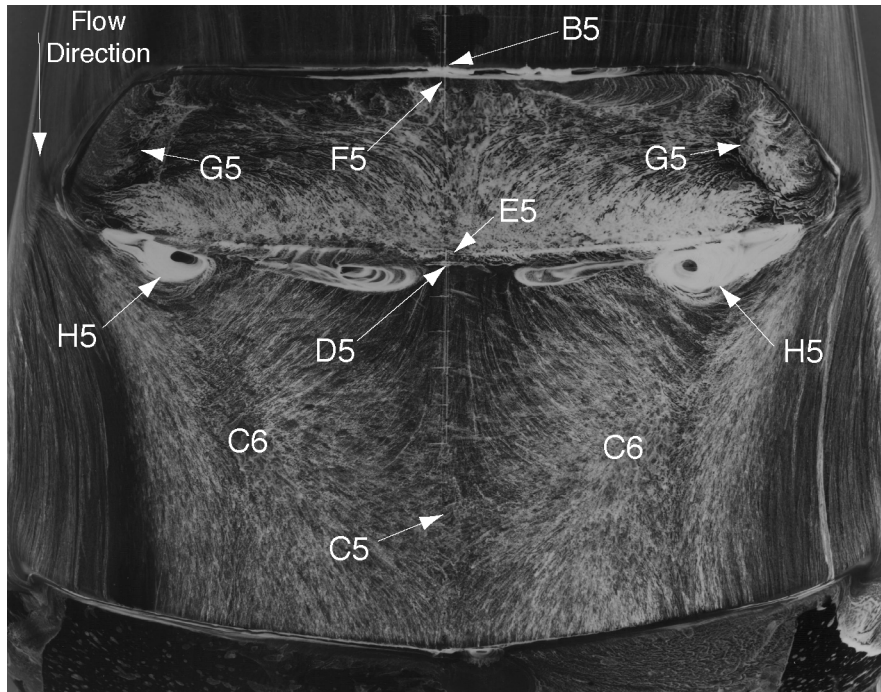


Figure 13. Surface flow pattern on the backlight and decklid.

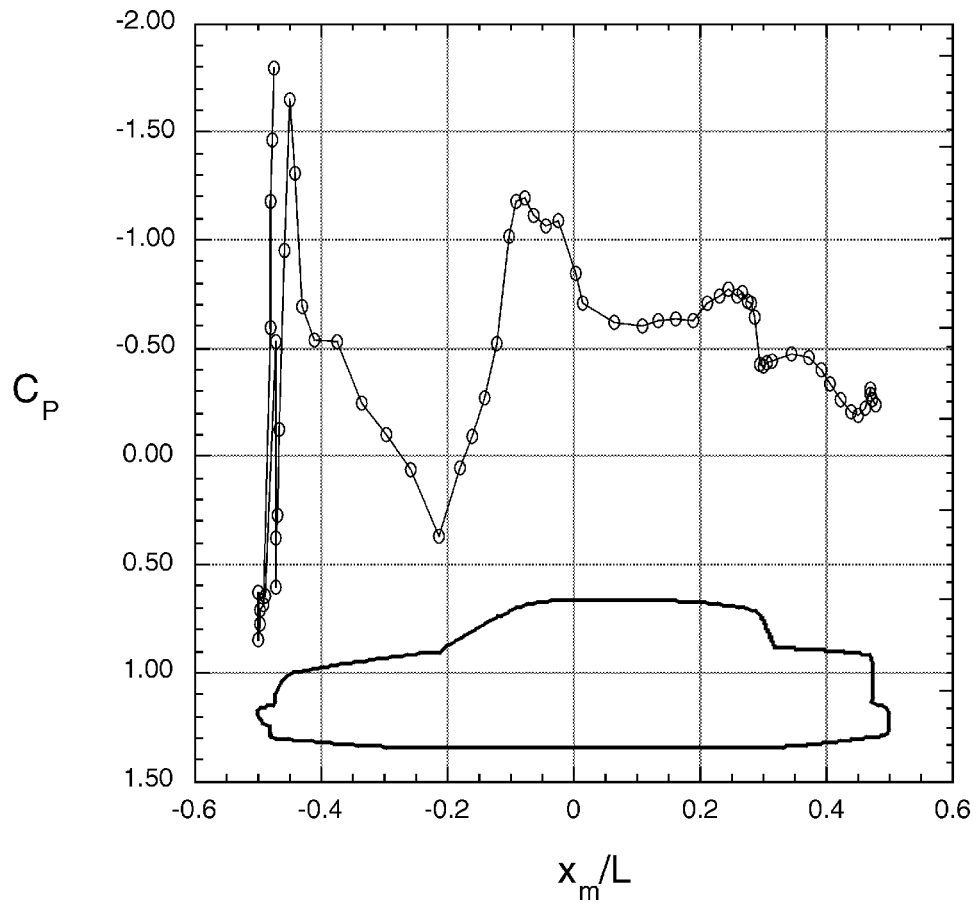


Figure 14. Centerline pressure distribution.

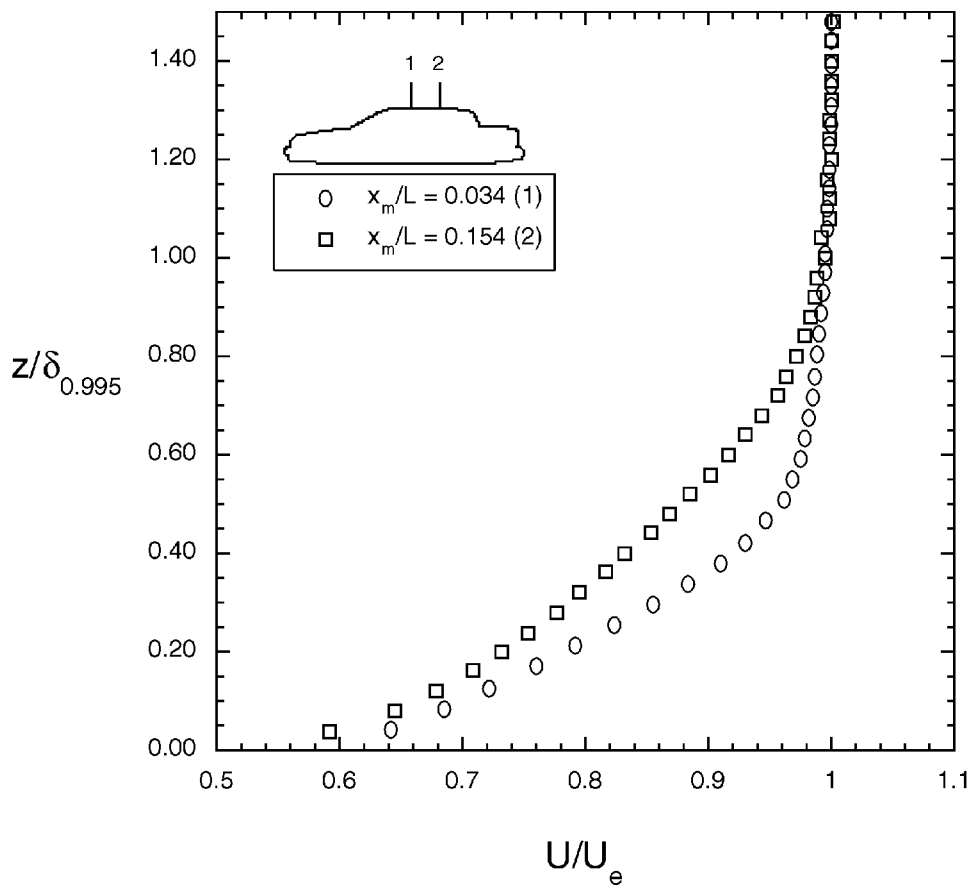


Figure 15. Profile comparison of the boundary layers measured on the car roof.

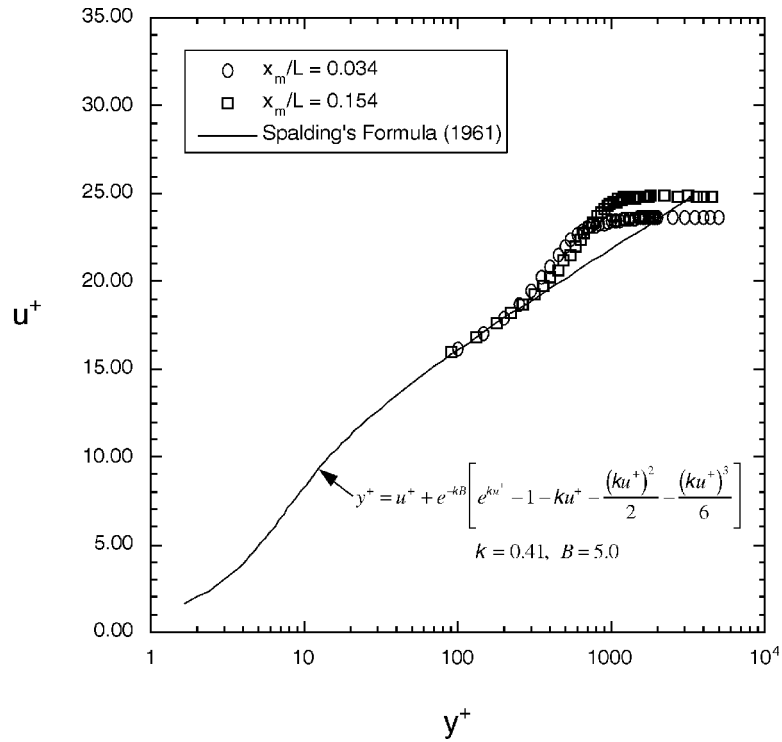


Figure 16. Comparison between measured boundary layer profiles and Spalding's formula.

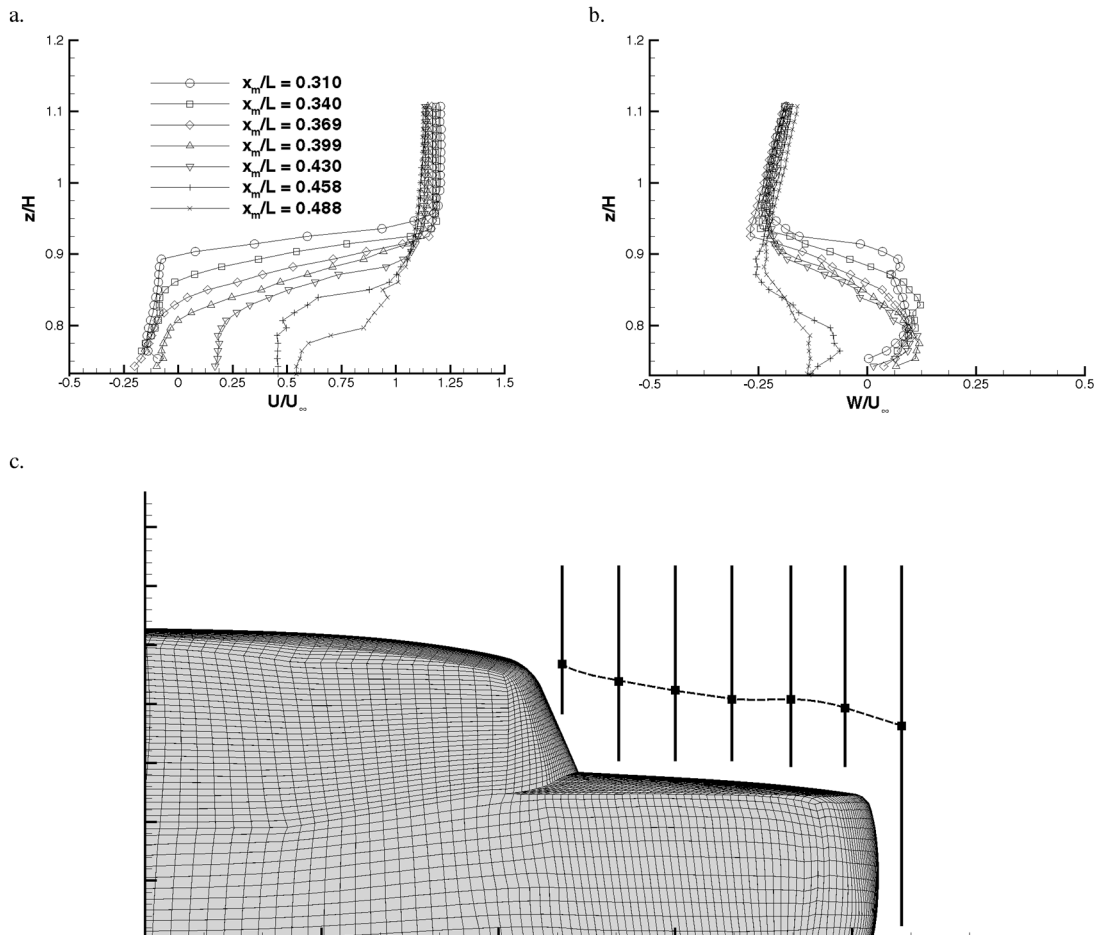


Figure 17. Center-plane velocities.

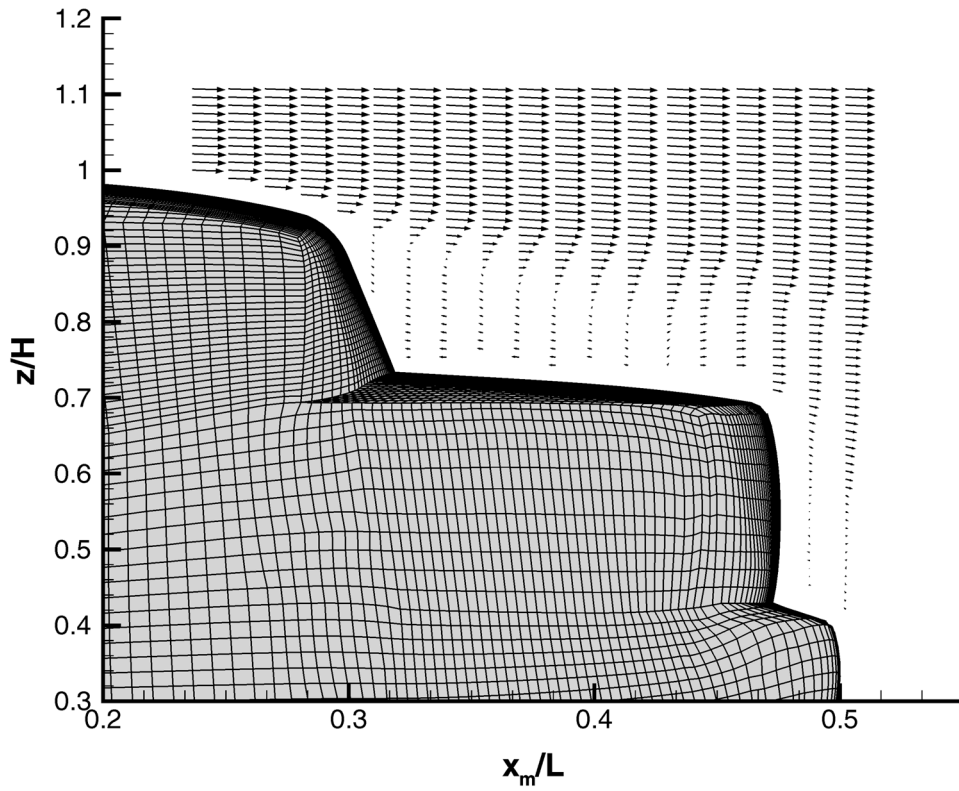


Figure 18. Center-plane velocity vectors.

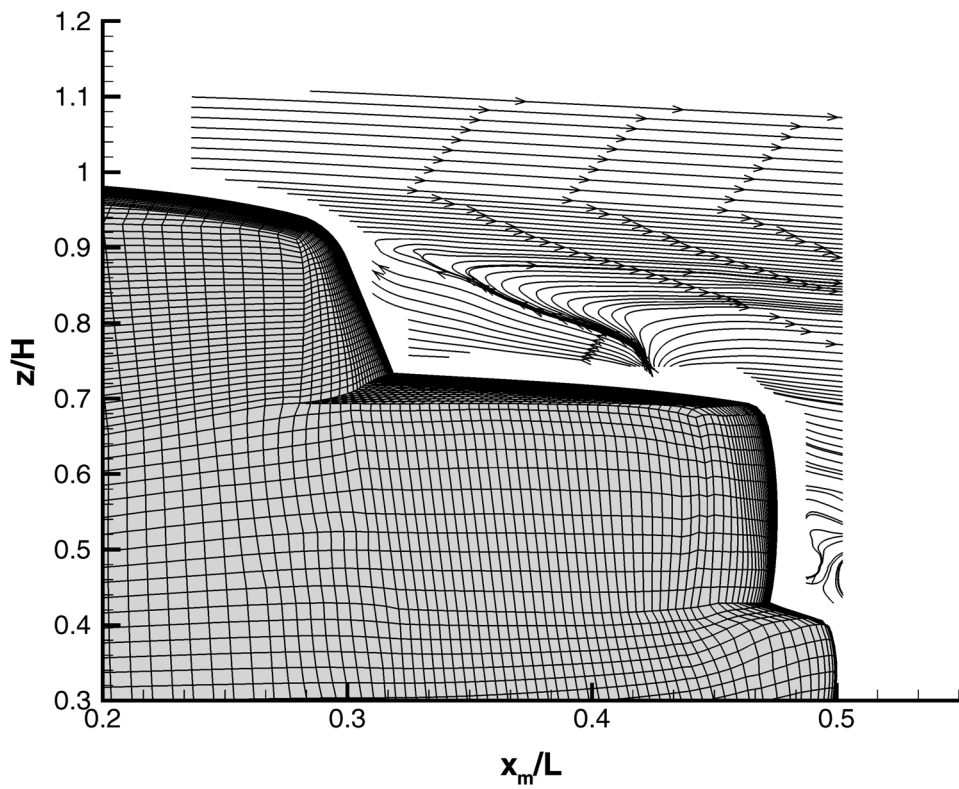


Figure 19. Center-plane streamlines.

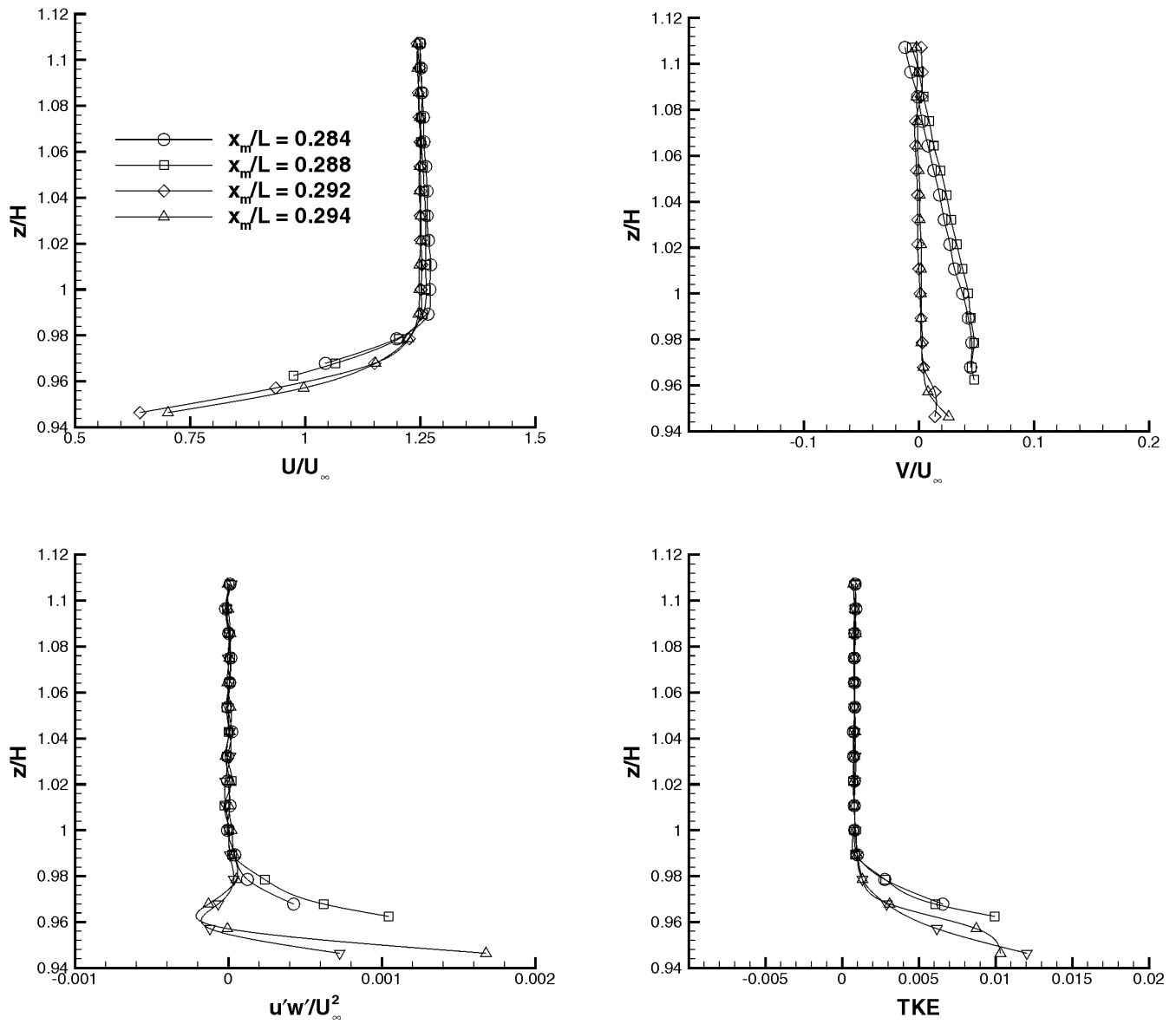
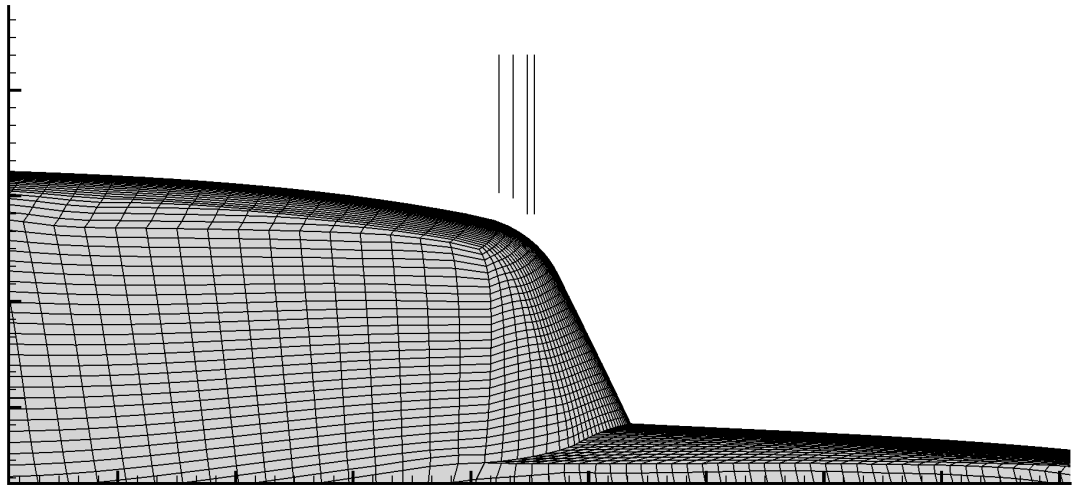


Figure 20. Comparison of selected mean velocities and turbulence quantities near the roof trailing edge.

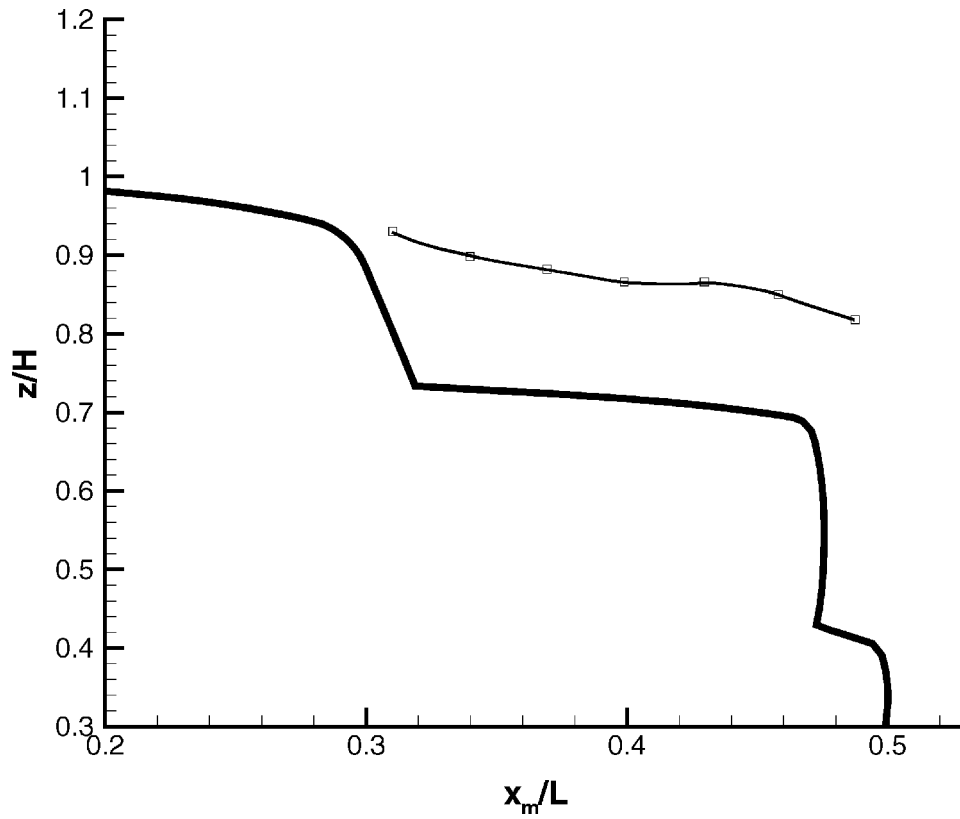


Figure 21. Deflection of the shear layer away from the deck lid.

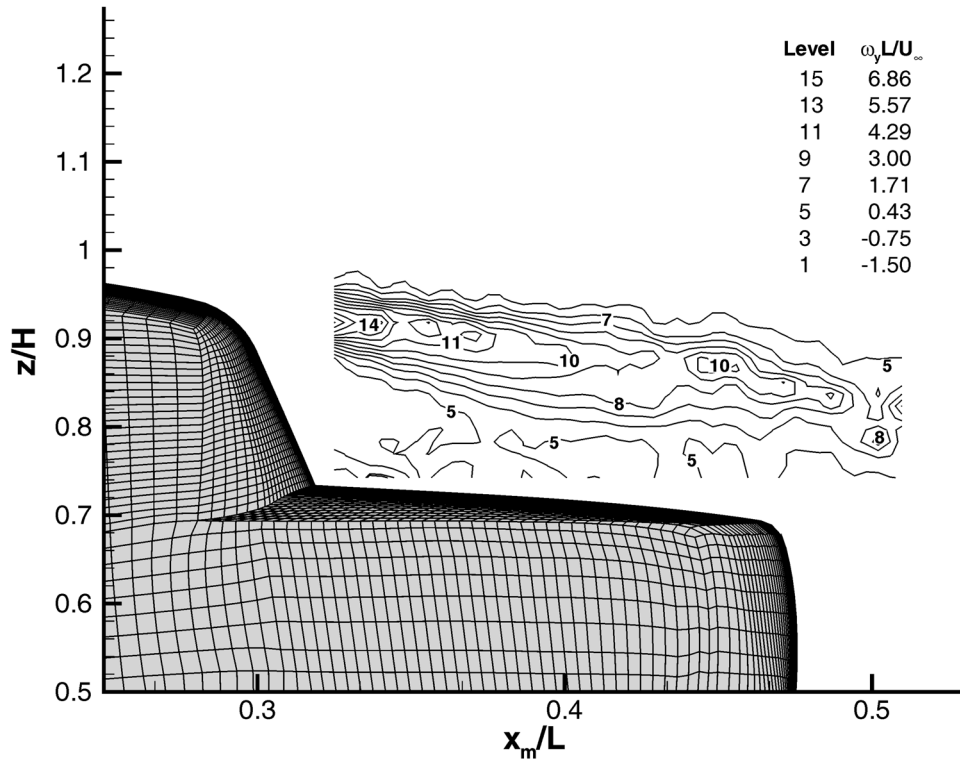


Figure 22. Transverse vorticity in the center plane.

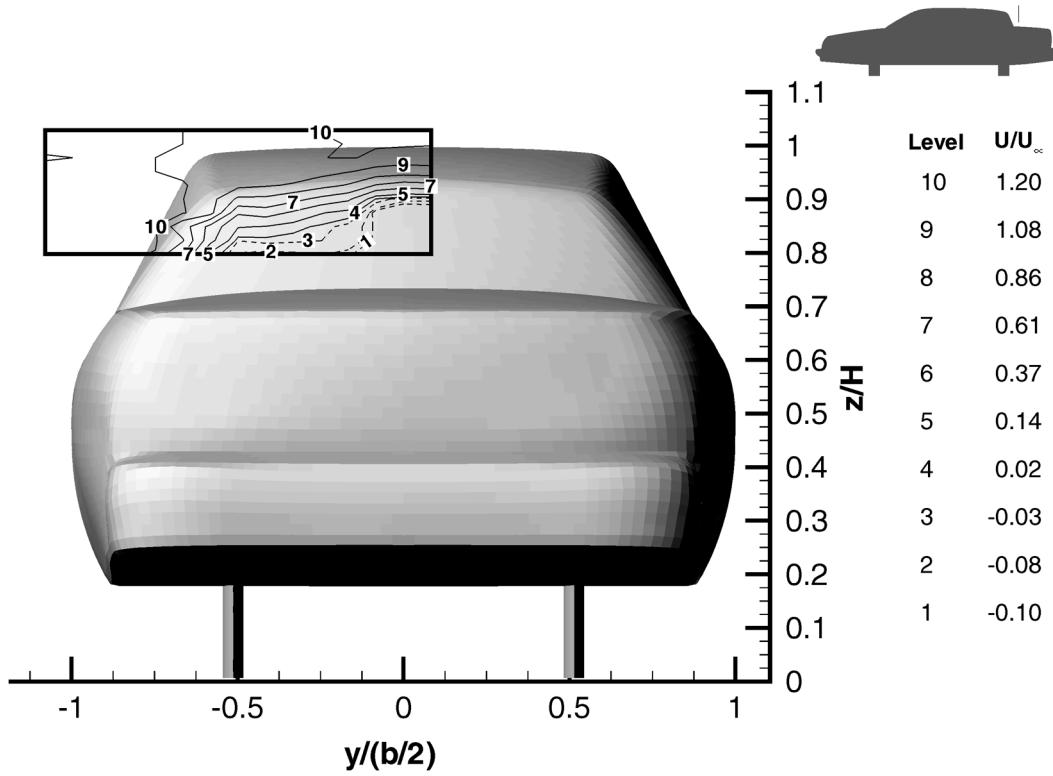


Figure 23. Contours of the streamwise velocity in a transverse plane at  $x_m/L = 0.340$ .

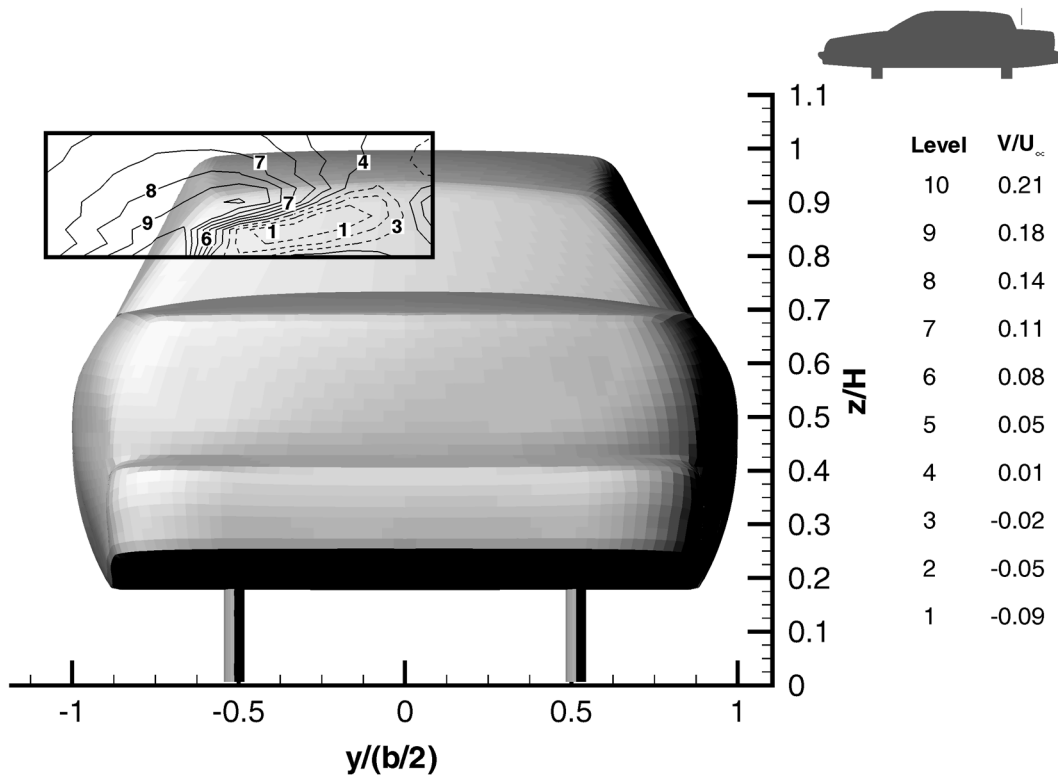


Figure 24. Contours of the transverse velocity measured in a transverse plane at  $x_m/L = 0.340$ .

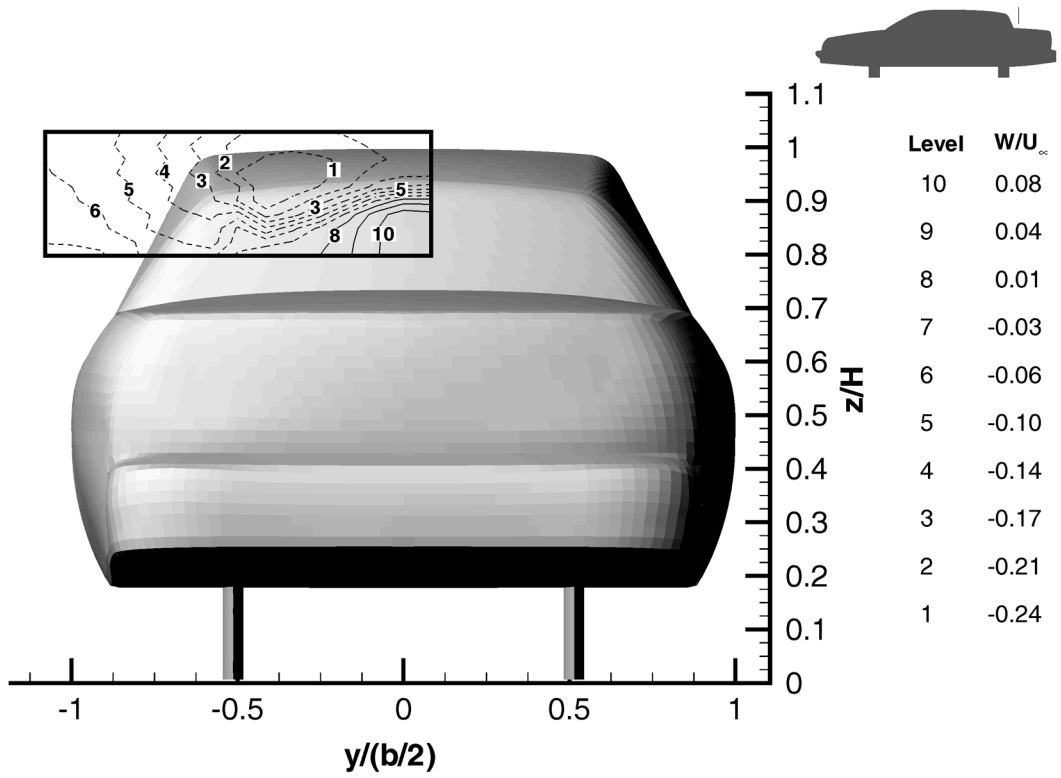


Figure 25. Contours of the vertical velocity measured in a transverse plane as  $x_m/L = 0.340$ .

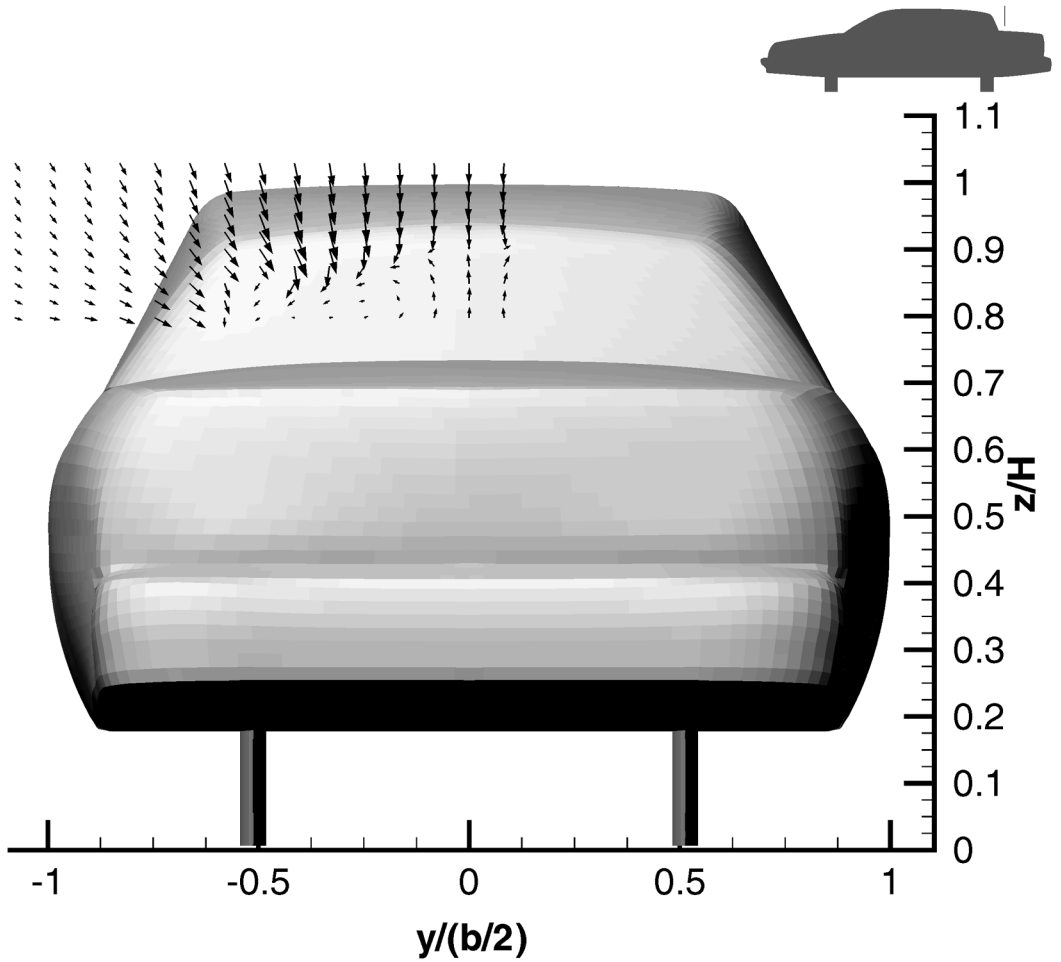


Figure 26. Velocity vector field in a transverse plane at  $x_m/L = 0.340$ .

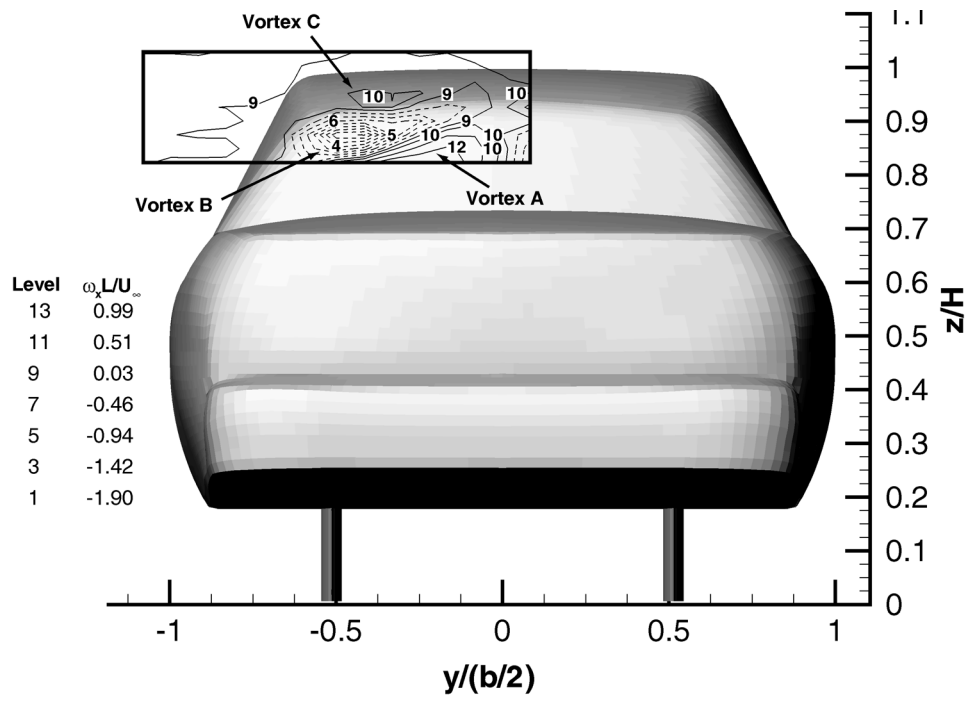


Figure 27. Streamwise vorticity in a transverse plane at  $x_m/L = 0.340$ .



Figure 28. Projected trajectory of the A-pillar vortex.

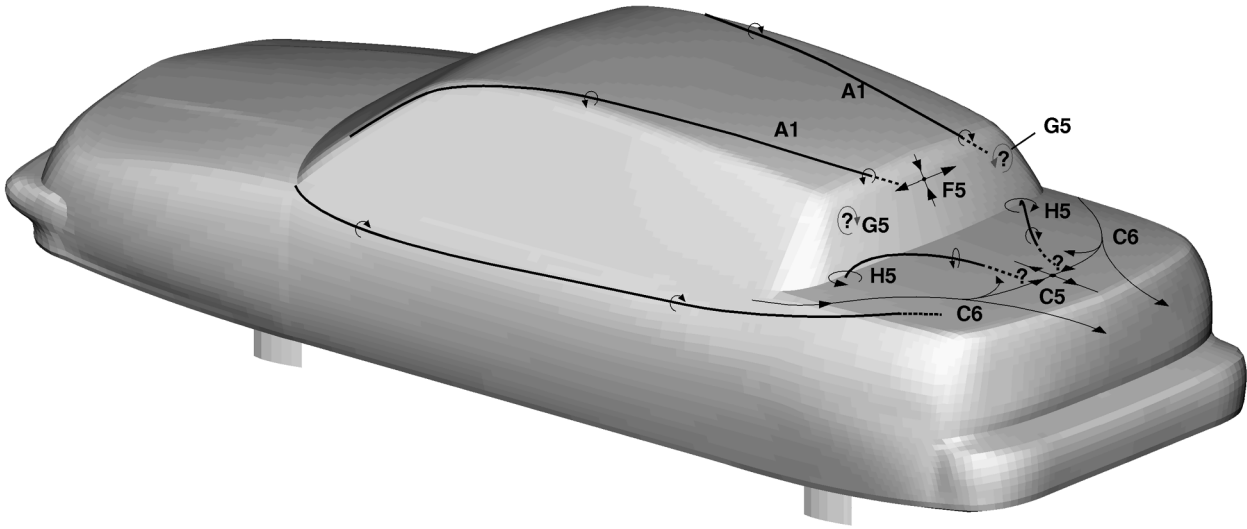


Figure 29. Flow structure deduced from the surface flow pattern and flow-field measurements.